SOLAR SELECTIVE OPTICAL COATING MADE

WITH METAL NANOPATICLES FOR

PHOTOVOLTAIC THERMAL

APPLICATIONS

by

XIN WANG

Presented to the Faculty of the Graduate School of

The University of Texas at Arlington in Partial Fulfillment

of the Requirements

for the Degree of

MASTER OF SCIENCE IN MATERIALS SCIENCE AND ENGINEERING

THE UNIVERSITY OF TEXAS AT ARLINGTON

December 2008

ACKNOWLEDGEMENTS

ABSTRACT

SOLAR SELECTIVE OPTICAL COATING MADE

WITH METAL NANOPATICLES FOR

PHOTOVOLTAIC THERMAL

APPLICATIONS

Xin Wang, M.S.

The University of Texas at Arlington, 2008

Supervising Professor: Michael Jin

The goal of this research is to fabricate solar selective reflector with suitable optical properties and high thermal and chemical stability for using in the photovoltaic thermal window. While the reflector allows some transmittance in visible spectrum, the mid/far infrared light needs to be reflected back into the window minimizing the IR radiation loss. Nickel/alumina composite was proposed as the solar selective reflector. This thesis consists of two parts - one part concerning the fabrication and characterization of solar selective reflector and another dealing with an optical modeling to simulate the optical properties of the solar selective reflector.

The alumina serves as a template for the formation of the oblated nickel nanoparticles, ca. 300nm in diameter with its length ranging from 109 to 245 nm. The Maxwell-Garnett theory was used to simulate the transmittance curve. The calculated curve shows fairly good agreement with the experiment data by considering the hole porosity due to some missing Ni particles in the composite and by defining an effective volume fraction from the experiment data.

iii

TABLE OF CONTENTS

LIST OF ILLUSTRATIONS

Figure   Page

vi

vii

LIST OF TABLES

ix

CHAPTER 1

INTRODUCTION

<u>1.1 Photovoltaic Thermal (PVT) System</u>

Solar energy is the most abundant permanent source in the world. It is found that about 170 trillion kW solar energy is intercepted by the earth every year (1). Solar energy is also a clean and environmentally compatible source of renewable energy. Other non-renewable fuels have many drawbacks. Their combustion produces pollution, acid rain, and global warming. According to the University of Miami's Clean Energy Research Institute, in 1996, the worldwide environmental damage caused by fossil fuel was about \$2,600 billion, which was about 14 % gross world product (2). There is no doubt that if we use clean energy such as solar energy, we will save the enormous money. Because of this it is important to develop an efficient solar energy conversion system to substitute the fossil fuel.

Photovoltaic thermal (PVT) system is one example of renewable energy conversion devices. The heart of the PVT system is a photovoltaic/solar-thermal conversion module in which a combination of photovoltaic cells with a solar thermal collector converts solar radiation into electricity and heat simultaneously. Apart from the PVT module other components including hot water storage tanks, heat exchangers, piping, controllers, inverters, wiring and heat pumps complete the PVT System.

PVT modules can generate more energy per unit surface area than side by side photovoltaic panels and solar thermal collectors (3), at a potentially lower production and installation cost. Moreover, PVT modules share the aesthetic advantage of PV. Because of their high efficiency per unit surface area, PVT is particularly well suited for applications with

both heat and power demand and with limited roof space available. Therefore, the potential of PVT is especially large in the residential market.

1.1.1 Typical Structure of PVT

Typical PVT system can be divided into 6 parts (Figure 1.1) (4). From top to bottom, they are the following:

- A laminate layer which is used to protect the whole PVT system.

- A photovoltaic panel which is used to absorb light energy and generate electricity and heat.

- An adhesive layer which connects PV panel and heat exchanger.

- A heat exchanger layer which is used for transfer the heat generated from PV panel to the water or air pipe.

- A water/ air pipe which absorbs the heat.

- An Insulating material which keeps the heat.
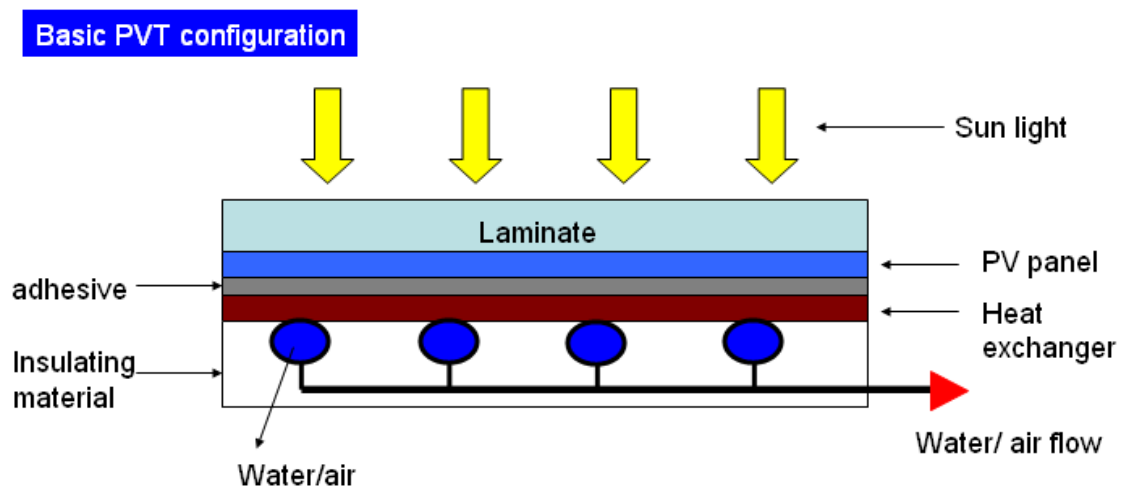
Figure 1.1 Basic photovoltaic thermal collector

2

<u>1.2 Solar Selective Absorber and Solar Selective Reflector</u>

A solar selective absorber is either a bulk material or a system of multilayer thin-film coating(s) that has high absorbance at wavelengths corresponding to that of the solar spectrum and low emittance in the infrared range. It can be a part of photothermal component in the PVT system (5) or it could simply a primary component of an independent solar thermal collector without PV part. Solar selective reflector is a thin-film coating designed to fully reflect light on certain wavelength range – primarily infrared light in this study. The solar absorber is also often referred as a system including both solar selective absorber and reflector coating on the surface confusing readers. Readers must pay attention to how the solar selective absorber is described in the article whenever they look up any reference.

Various kinds of spectrally selective thin-film coatings exist. Four major types of solar selective absorber/reflector can be found in the literature (6-8); intrinsic, textured surface, tandem, and a heat-mirror type. The following sections describe solar and black body radiation together with four kinds of solar selective absorber/reflector.

1.2.1 Solar and Black Body Radiation

The optical design of an absorber together with its solar selective coating on the surface is determined by the spectral distribution of solar and thermal radiation. Terrestrial solar radiation spectrally confined between 0.3 to 2.5 μm amounts for 98.5 % of the total incoming solar radiation, and the maximum solar intensity is found at around 0.55 µm. The whole solar spectrum can be viewed in Figure 1.2 (9) - observe that the X axis is logarithmic. When a surface becomes warmer than the surroundings, it has a net radiation transfer to the surroundings. Thermal radiation is usually referred to as blackbody radiation, i.e. the maximal radiation to be emitted for a certain temperature. The blackbody radiation distributions at the temperatures 100, 200 and 300 ⁰C are illustrated in the figure. The temperature of an absorber in operation under normal conditions is typically less than 100 ⁰C. The sun's radiation spectrum

is found to lie in the wavelength interval $0.3\ \mu m \leq \lambda \leq 2\mu m$ where high absorption is desired. At $\lambda \geq 2\mu m$ the high reflectance is desired to minimize the radiative heat loss.
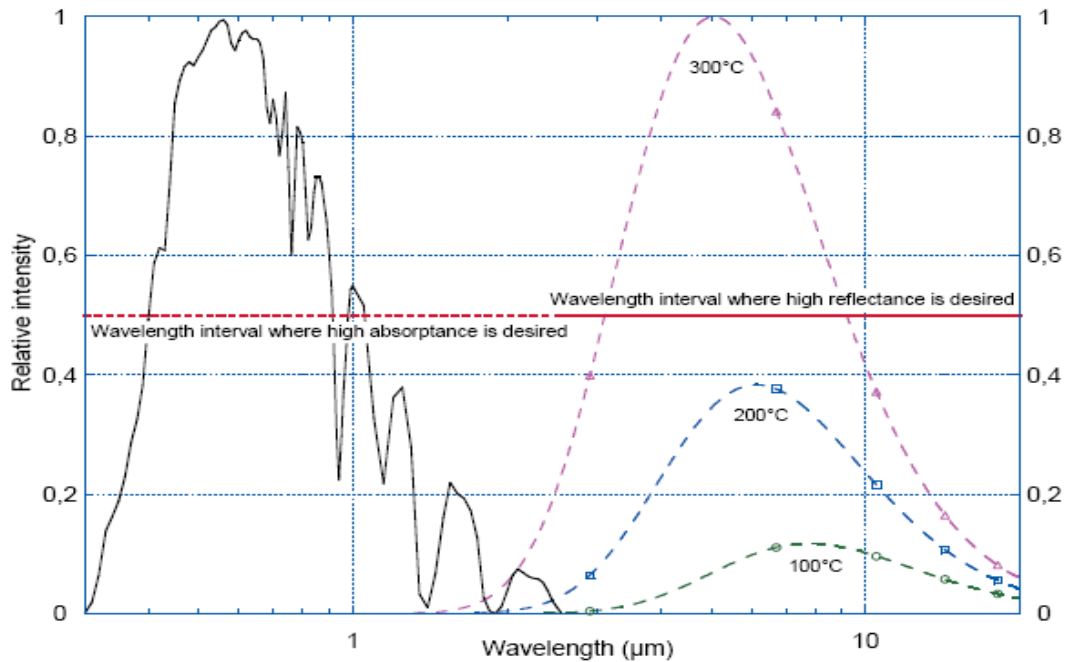
Figure 1.2 The solar irradiance distribution curve (ISO standard 9845-1) (solid), and the emitted radiation curves of blackbodies at 100, 200 and 300 ºC (dashed). The figure indicates the wavelength intervals where high absorption and high reflectance are desirable respectively for the absorber and its solar selective reflective coating on the surface (9).

1.2.2 Intrinsic Selective Reflection Coating

This is the most straightforward type of selective surface. It consists of a single substance with intrinsic optical properties that are wavelength selective. However, the threshold from low to high reflectance either occurs often at the wrong wavelength or is not sharp enough, and so far, research on this type of material has not succeeded in creating a commercial product. The best coating of this type, up to now, is made of ZrB_2 (10). Coating of ZrB_2 for photothermal solar absorber applications was prepared using chemical vapor deposition (CVD)

techniques. In the non optimized sample the absorption of ZrB_2 is 0.67-0.77 while emittance is 0.08 -0.09.

1.2.3 Textured Surfaces

Special rough surface textures can be very efficient at trapping light increasing absorption. Hence these types of coatings are also called optical trapping surfaces. The part of the light that is not immediately absorbed in the surface is reflected deeper in between the surface dendrites and another portion is absorbed the next time it strikes the surface. These multiple reflections can lead to a high solar absorption (7). The long-wavelength emittance is practically unaffected by this texture.

1.2.4 Tandem Structure (12-15)

These tandem selective spectrum coatings consist of two different surfaces, each with unique optical properties. Together they can exhibit a far greater spectral selectivity compared to what an intrinsic absorber could theoretically achieve. The easiest way of obtaining the desired optical properties is to create an absorber-reflector tandem. This type of absorber, which is also called a dark mirror, is made of a substrate with high infrared reflectance, i.e. low thermal emittance. Metals such as aluminum, copper, nickel, steel and, silver fulfill this criterion. A thin film is often added on top of the substrate, and the film should be highly absorptive in the solar wavelength interval and highly transparent in the infrared wavelength interval. Commercially available high performing absorber-reflector tandems have been constructed using sputtered, electroplated, anodized or evaporated surface coatings which can be either metal or semiconductor on metal substrates. Several possible combinations of materials for constructing an absorber-reflector tandem are available.

1.2.4.1 Paint Tandem

This tandem type of absorber utilizes inorganic pigments dispersed in a resin to capture solar radiation (11). It is an inexpensive and simple way of creating a solar selective absorbing

surface. Up until 2006, there has been a significant disadvantage in using this kind of absorber; the normal thermal emittance value is very high compared to the thin film metal-dielectric compounds.

1.2.4.2 Multi-layer/Metal Tandems

An efficient spectrally selective solar absorbing surface can easily be tailored by using a multi-layer design. A multi-layer is constructed out of several alternate layers of semitransparent metal and dielectric materials. One example is an $Al_2O_3/Mo/Al_2O_3$ triple layer. Sputtering techniques are generally used to deposit this type of coating. (14)

1.2.4.3 Metal-Dielectric Composite/Metal Tandems

This absorber normally consists of metal or metal oxide nano-particles embedded in a dielectric matrix. A major advantage of this cermet (ceramic-metal) is that it offers a high degree of flexibility - by varying the choice of particle, particle size, particle orientation and shape, film thickness, and particle concentration in the film, various spectral selectivities can be created. Alumina and polycarbonate are widely used as dielectric material. Electroplating, sputtering, anodization, chemical vapor deposition, and evaporation are some of the techniques previously used to produce these composite coatings (15).

1.2.4.4 Semiconductor/Metal Tandems

A semiconductor/metal tandem utilizes the fact that semiconductors exhibit specific band gaps. High quality solar selective absorber requires that all radiation with a wavelength shorter than 2.5 μm be absorbed. This demand corresponds to a semiconductor material with a band gap of 0.5 eV. Though some research has been done in this area, commercially interesting product has not been found because most semiconductors have a band gap larger than 0.5 eV. PbS is a good choice with a band gap of 0.4 eV, but its toxicity is a concern

1.2.5 Heat-Mirror on Black Substrate

A heat-mirror on black substrate absorber makes use of the tandem idea, but in an opposite way. The coating (heat-mirror) needs to be highly reflective in the infrared wavelength

interval and at the same time transparent to wavelengths in the solar spectrum. The substrate is selected to be a nonselective absorber with long-term durability properties. SnO_2:F on a substrate of black enamel is one of the previously investigated absorbers of this type (13).

1.3 Objective

While this thesis is focusing on the optical analysis of one of the model experiments related to the solar selective reflection coating, the ultimate practical goal of the technology is to fabricate PVT window which generates both electricity and heat while it allows some visible light to pass through for the functionality of conventional window. Potential application for PVT window would be building-integrated applications.

Two important modifications from more conventional, visibly opaque PVT system (Figure 1.1 as an example) includes (i) making a visibly semi-transparent solar cell to harvest a part of solar spectrum and (ii) devising a visibly semi-transparent selective absorber photothermal component (an absorber with a reflective coating) to harvest only a part of the solar spectrum. While creating the semi-transparent solar absorber is critical, it is another challenge to make the efficient semi-transparent reflective coating. This coating will substitute the insulating material in Figure 1.1 since the insulating layer will absorb the most of the visible light. Figure 1.3 shows the conceptual schematic of PVT window – transparent medium that can absorb radiative IR needs to be devised and included in the picture to be complete. Again, this thesis studies the optical analysis of the model experiments focusing on the nano-structured solar selective coating and will be explained in details in the following sections.
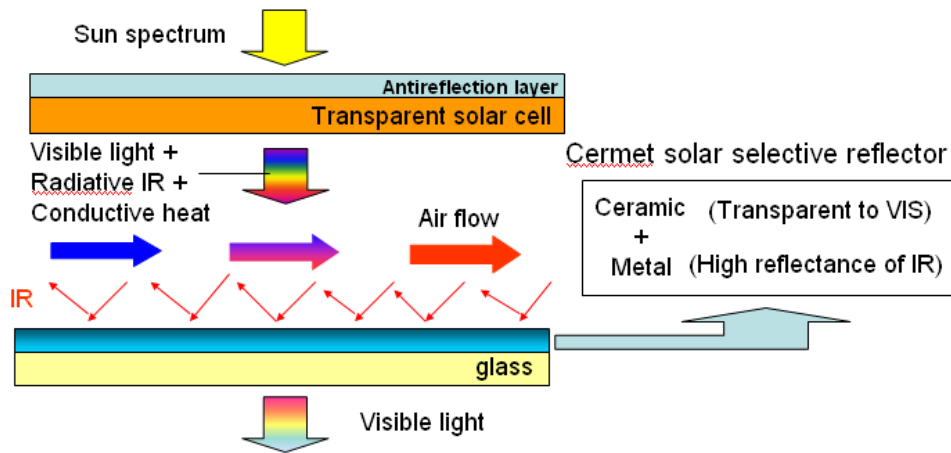
Figure 1.3 Conceptual schematic of PVT window

Figure 1.4 graphically summarizes the optical characteristics of one of the opaque selective absorbers studies in the field previously (16). The structure has thick aluminum layer which is several micrometers on the backside to reflect the infrared light. The alumina is filled with nickel particles which are ten to hundred nanometers in diameter and 1 μm in length. The surface of the structure has a very desirable reflectance characteristic of solar selective reflector having the wavelength threshold at around 2 μm and all the literature stressed the importance of nanostructured cermet (alumina-nickel) structure on the surface. Certainly the transmittance is expected to be very minimal in most spectral range of interest due to the thick Al substrate. It is our finding though that the previous studies seldom characterized the optical properties of the cermet structure separately from Al substrate and left a lot of fundamental questions unanswered.

8
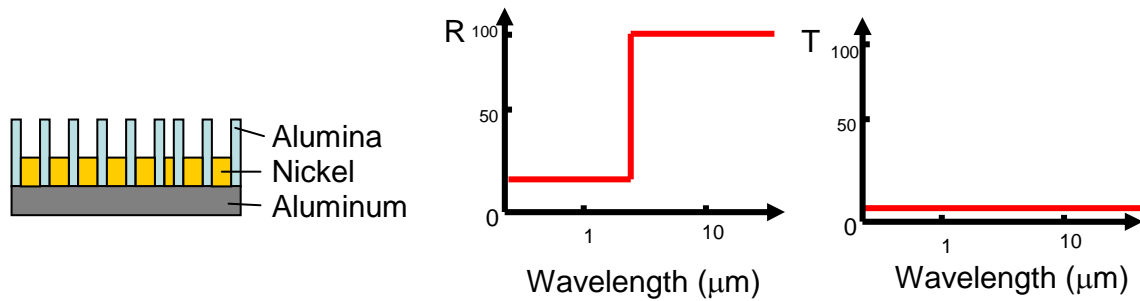
Figure 1.4 Typical nickel alumina aluminum tandem selective absorber and its optical characteristics.

Our model structure of selective reflector for PVT window and its speculated optical characteristics are shown in Figure 1.5. By removing thick metal substrate and by controlling the size of metal particles embedded in alumina from Figure 1.4, the increase in transmittance of visible light and the loss in reflectance are expected. For the cermet structure, nickel and alumina have been chosen to compare with existing studies with metal substrate. This study will theoretically analyze the optical data collected using effective medium theory to provide more insight in the cermet structure. The effective medium theory is more thoroughly described in section 1.5. The Ni-Al_2O_3 composites chosen as a model system here provide much convenience for evaluating theoretical approaches because the nano-structured alumina oxide structure from well-established technology can provide the necessary versatility of controlling size and shape of the metal particles embedded. In order to fabricate the reflector, the electrodeposition of nickel nanoparticles into the alumina was performed. The following section will provide the basic principle of the electrodeposition.

9
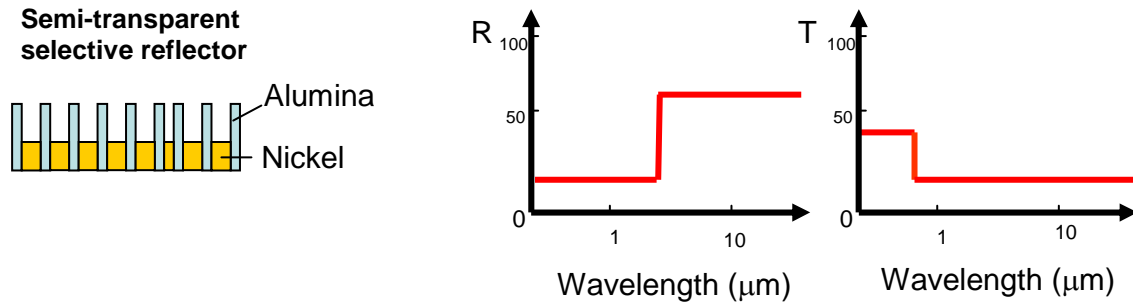
Figure 1.5 Model selective reflector and its speculated optical characteristics.

1.4 Electrodeposition

Electrodeposition is the process of using electrical current to reduce cations of a desired material from a solution and coat a conductive object with a thin layer of the material such as a metal, for example. The layer bestows a desired property (e.g., abrasion and wear resistance, corosion protection, aesthetic qualities, etc.) to a surface that otherwise lacks the property.

It is analogous to a galvanic cell acting in reverse. The part to be plated is the cathode of the circuit. In one technique, the anode is made of the metal to be plated on the part. Both components are immersed in a solution called an electrolyte containing one or more dissolved metal salts as well as other ions that permit the flow of electricity. A rectifier supplies a direct current to the cathode causing the metal ions in the electrolyte solution to lose their charge and plate out on the cathode. As the electrical current flows through the circuit, the anode slowly dissolves and replenishes the ions in the bath. A simple electrodeposition system consists of the following components:

10
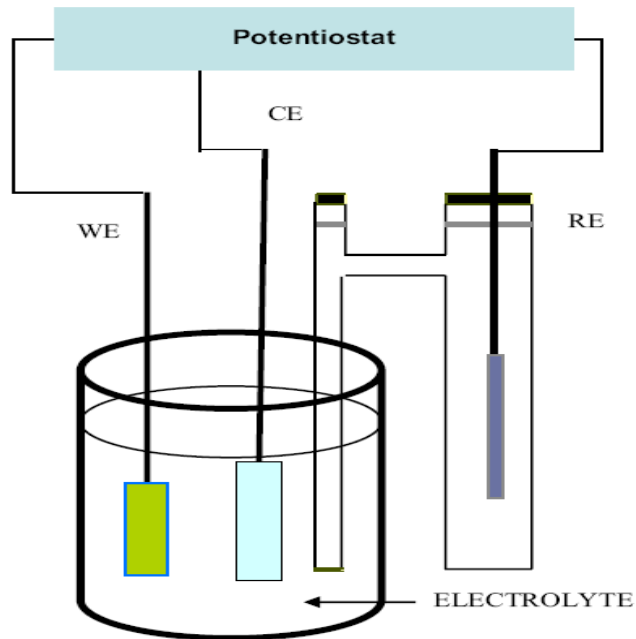
Figure 1.6 Standard set up for potentiostaic electrodeposition.

-Electrolyte: The electrolyte or bath provides the ions to be deposited. It could be aqueous, non-aqueous or molten. It should be electrically conductive and must contain the appropriate precursors, e.g., metal salts, organic monomers, etc.

-Electrodes: The electric field, which provides the main driving force for the deposition, is applied between two electrodes, the anode (oxidizing electrode) and the cathode (reducing electrode). Cathodic deposition is generally more popular when depositing metals or metal oxides since (a) most metal ions are positive ions and (b) anodic deposition often produces films with poor stoichiometry and adhesion. A third, reference electrode is used especially during potentiostatic depositions (see Figure 1.6) to maintain constant potential.

11

-Power supply: The power supply could be (a) a direct current at constant voltage, which leads to potentiostatic electrodeposition, or (b) a direct constant current, which leads to galvanostatic electrodeposition, or (c) a current or voltage waveform or pulse.

Electrochemical techniques offer a number of advantages over chemical routes some of which are stated below:

-Electrochemical reactions are much cleaner than chemical reactions.

-Economical considerations often favor the electrochemical route over existing chemical processes

-There are a number of examples where electrochemical routes produce unique products and do so in reaction pathways which themselves are unique

-Electrochemical routes can be controlled exceptionally well by means of electrode potentials and electrode materials, to give a high selectivity of the desired product

-The same reactor can sometimes be used to produce useful products at both the cathode and the anode

1.5 Optical Analysis of Optical Selective Coating Using Effective Medium Theory

Fabricating a well-designed spectrally selective absorbing surface requires understanding of basic electromagnetic wave theory. The following section describes how electromagnetic waves interact with matter in thin films (17-20).

1.5.1 Electromagnetic Radiation and Optical Constants

A plane electromagnetic wave propagating along the x-axis through an absorbing medium at time *t* is described by its electric field component, *E(x,t)*,

$$E = E_0 \exp(-k\omega x / c + i(n\omega x / c - \omega t)) . \tag{1.1}$$

E_0 is the amplitude of the electromagnetic wave with an angular frequency of ω before it enters the medium. The speed of light in vacuum is denoted as c. The complex refractive index is given by equation 1.2,

$$N = n + ik .$$ (1.2)

The real part of the refractive index is denoted as n, which relates to the phase of the wave. The imaginary part is noted as κ (also called as an extinction coefficient), which describes a damping of the amplitude in the direction of propagation. The intensity of the light is proportional to E^2 which leads to Beer's law that describes the change in intensity (I) of an electromagnetic wave as a function of travel distance, x when propagating through a medium,

$$I = I_0 \exp(-\alpha x)$$ (1.3)

where I_0 is the intensity of light before entering the medium and α represents the absorption coefficient. Combining equations 1.1 and 1.3, α is identified as

$$\alpha = \frac{2k\omega}{c} = \frac{4\pi k}{\lambda} .$$ (1.4)

The angular frequency ω can be expressed as equation 1.5 where λ is the wavelength of light in vacuum.

$$\omega = \frac{2\pi c}{\lambda} .$$ (1.5)

We can relate the refractive index of a medium to its relative dielectric constant ε_r by using the standard result derived from Maxwell's equation,

$$N = \sqrt{\overset{\circ}{\varepsilon_r}} .$$ (1.6)

We can define the complex relative dielectric constant $\overset{\circ}{\varepsilon_r}$ according to

$$\overset{\circ}{\varepsilon_r} = \varepsilon_1 + i\varepsilon_2 .$$ (1.7)

Now we can work out explicit relationships between the real and imaginary parts of N and $\overset{\circ}{\varepsilon_r}$ by combining equations 1.2 and 1.7. These are

$$\varepsilon_1 = n^2 - k^2 \tag{1.8}$$

$$\varepsilon_2 = 2nk \tag{1.9}$$

and

$$n = \frac{1}{\sqrt{2}}(\varepsilon_1 + (\varepsilon_1^2 + \varepsilon_2^2)^{\frac{1}{2}})^{\frac{1}{2}} \tag{1.10}$$

$$k = \frac{1}{\sqrt{2}}(-\varepsilon_1 + (\varepsilon_1^2 + \varepsilon_2^2)^{\frac{1}{2}})^{\frac{1}{2}} . \tag{1.11}$$

1.5.2 Effective Medium Theory

For inhomogeneous composite media consisting of small particles hosted in a dielectric matrix, the optical constants can be derived from the optical constants of the homogeneous constituents. If the size of the inhomogeneties is much less than the wavelength of the incident light, the electric and magnetic fields are almost constant over this characteristic length, which is the quasi-static approximation. We then describe the response of a material to an electromagnetic field by the dielectric function and magnetic permeability. In the solar and infrared wavelength regions, the magnetic permeability approaches unity and the optical properties can be treated with an effective dielectric function of the medium on the basis of effective medium theory (EMT) (21).

The most commonly used effective medium theories are the Maxwell-Garnett (MG) (22) and Bruggeman (BR)(23). They can be used to model the effective dielectric function of the composite coating for spherical inclusions and the effective quantity depends only on the dielectric functions of the components and their volume fractions. The MG theory, in its simplest

14

form, assumes that the medium has a separated grain structure (Figure. 1.7(a)). The BR theory assumes a two component mixture having aggregate microstructure (Figure. 1.7(b)).

To derive the effective dielectric function, each particle in the composite is considered to be embedded in an effective medium and the composite can be of two or higher component systems. Here we deal with two components of dielectric constants ε_a and ε_b on the work of Niklasson *et al.* (8) using the microstructures of Figures 1.7(a) and 1.7(b). The calculation has been simplified by using the random unit cell of Figures 1.7(c) and 1.7(d) that properly accounts for the essential features of the separate and aggregate microstructures, respectively
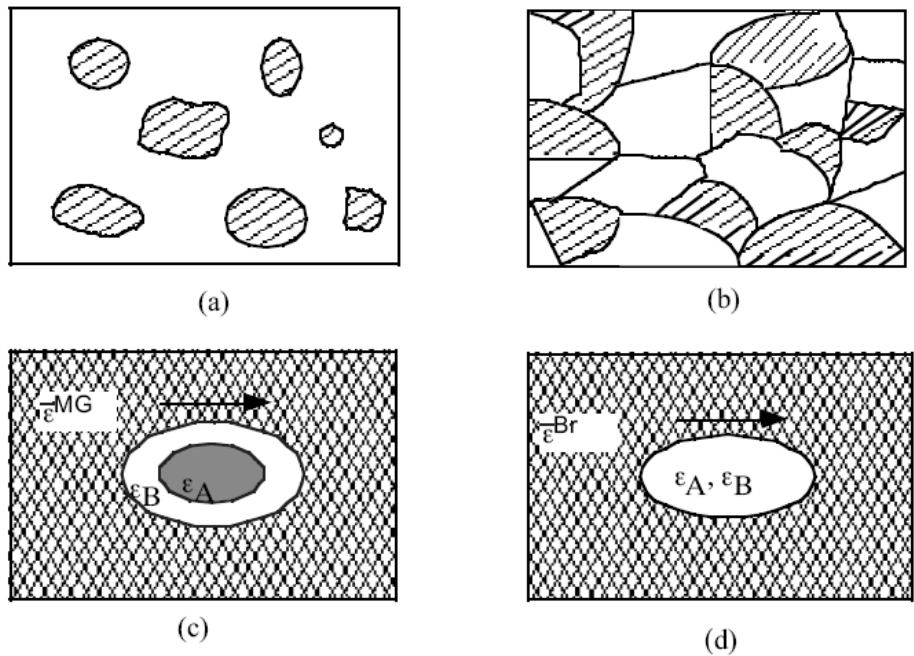
Figure 1.7 Microstructure of (a) separated grain (b) aggregate structures for a two component medium, (c) and (d) are random unit cells to derive the effective dielectric function of the separated grain (MG model) and aggregate (BR model) structures, respectively. The arrow indicates the direction of the polarized light.

15

1.5.2.1 The Maxwell-Garnett and Brugggeman Theories

The general relationship between the composite's effective dielectric function ε and the dielectric functions of the metal component ε_m and the insulating component ε_0 is based on an extension of the Clausius-Mossotti equation (11, 21).

$$\frac{\varepsilon - \varepsilon_h}{\varepsilon + \kappa \varepsilon_h} = f_m \frac{\varepsilon_m - \varepsilon_h}{\varepsilon_m + \kappa \varepsilon_h} + f_0 \frac{\varepsilon_0 - \varepsilon_h}{\varepsilon_0 + \kappa \varepsilon_h} \tag{1.12}$$

where f_m and f_0 are the volume fractions of the metal and insulator, respectively. The screening parameter κ depends on the shapes of the component particles and the orientation of these particles with respect to the electric field. This factor will be discussed further below.

The host function ε_h, describes the dielectric constant experienced by the component particles at the microscopic level. The MG model assumes that at all metal volume fractions, the metal particles are surrounded by a layer of insulating material. Hence, ε_h is assumed to be equal to ε_0. Equation 1.12 then reduces to

$$\frac{\varepsilon - \varepsilon_0}{\varepsilon + \kappa \varepsilon_0} = f_m \frac{\varepsilon_m - \varepsilon_0}{\varepsilon_m + \kappa \varepsilon_0} \tag{1.13}$$

In contrast, the BR treatment assumes that the composite contains a random mixture of metal and insulator particles. The host function cannot be identified with ε_0 because at some critical volume fraction of metal, the metal particles must begin to touch each other. In this case, then, ε_h is assumed to be equal to ε. Equation 1.12 thus becomes

$$f_m \frac{\varepsilon_m - \varepsilon}{\varepsilon_m + \kappa \varepsilon} + f_0 \frac{\varepsilon_0 - \varepsilon}{\varepsilon_0 + \kappa \varepsilon} = 0 \tag{1.14}$$

1.5.2.2 Screening Parameter and Particle Shape.

The screen parameter κ indicates the amounts of "screening" that takes place in a composite and is a function of the particle shape, size, and orientation of the material. The

screening parameter is an indication of transparency. The calculation of κ depends on the depolarization factor q as follows (21),

$$\kappa = \frac{1-q}{q}.$$ (1.15)

The depolarization factor is the ratio of the internal electric field induced by the charges on the surface to the polarization of the dielectric when an external field is applied. The depolarization factor depends on the geometry of the particle and its orientation with respect to the electric field. In the work we assume the nickel nano-cylinder can be treated as ellipsoids as shown in the Figure 1.8. The depolarization factor is related to the eccentricity f and the eccentricity is the measure of how much an ellipsoid deviates from the shape of a sphere. For an oblated particle, eccentricity is equal to

$$f^2 = \frac{b^2 - a^2}{a^2}.$$ (1.16)

Here a is the semi minor length of the particle and b is the radius of the particle and then the depolarization factor is equal to (24)

$$q = \frac{1+f^2}{f^2}[1 - \frac{1}{f}(\arctan f)].$$ (1.17)
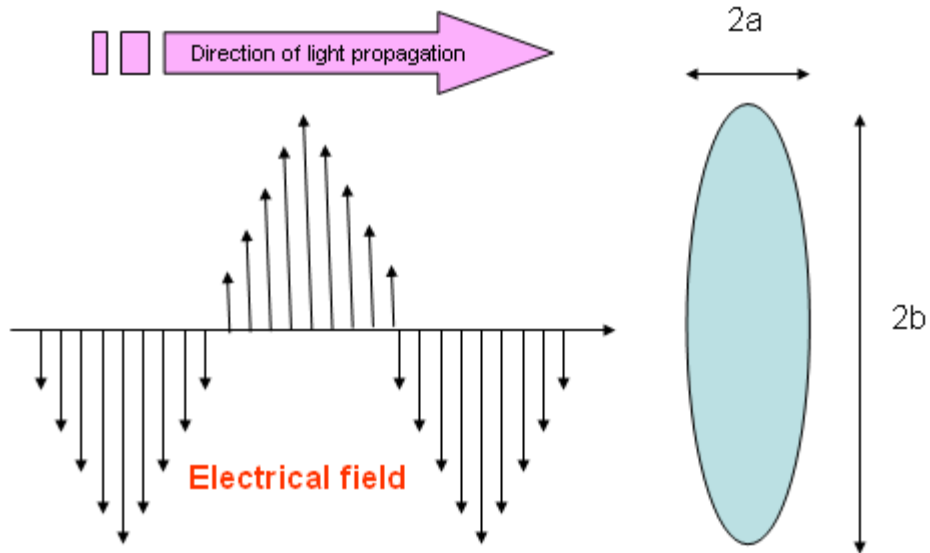
Figure. 1.8 Orientation of an ellipsoid of revolution with respect to electric field and axes relevant to the estimation of the depolarization factor q.

1.5.3 Optical Characterization of a Solar Selective Coating

Consider a ray of light impinging on a thin film. When the ray reaches the surface it is partly reflected at the front surface, absorbed in the film and/or transmitted through the film. The energy conservation in the interaction between the medium and the radiation is described by equation 1.18 where A is the spectral absorptance, R the reflectance, and T the transmittance,

$$R(\lambda) + A(\lambda) + T(\lambda) = 1. \tag{1.18}$$

In our study the microstructure of our solar selective coating can be modeled as shown in the Figure 1.9 where d_2 is the average thickness of the composite layer containing nickel nano-cylinders, and d_1 and d_3 are the average distances from the composite region to the membrane faces. This three layer model (metal- free region of thickness d_1, metal containing region of thickness d_2 and metal- free region of thickness d_3) is the basis for the analysis using EMT.

18
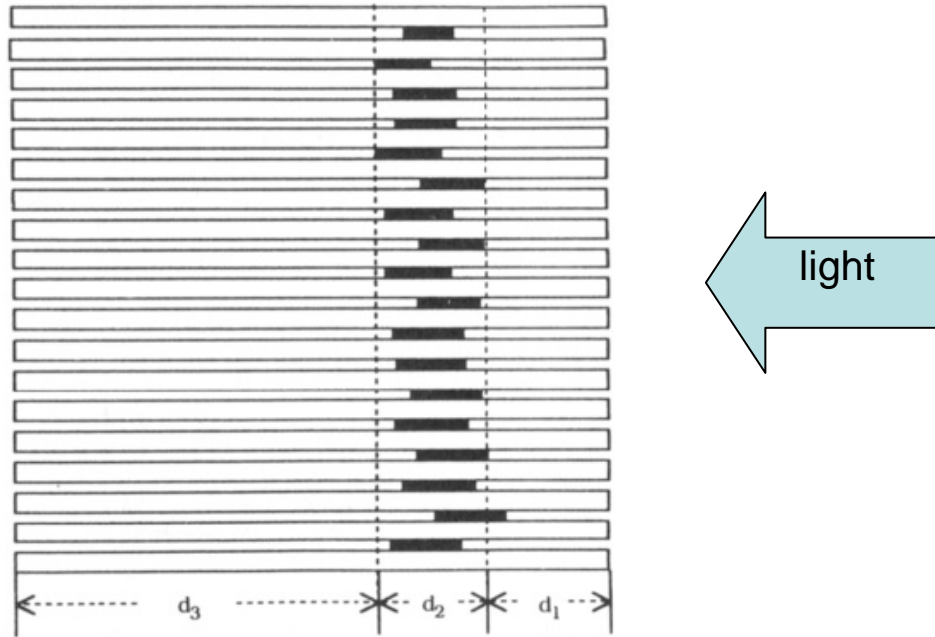
Figure. 1.9 Three layer model for nickel alumina composite systems employed in spectral simulation.

Microscopic analysis of the composite membranes and the free nickel particles indicates that the nickel particles are isolated from each other by the pore walls of the host oxide. Hence the MG formulation of EMT should be more appropriate. In the case, the calculation involves resolving the given EMT expression (ε from eq 1.13) into its real and imaginary components using equations 1.8 and 1.9 respectively. The optical constants, n_m and k_m for nickel were taken from (25). Optical transmittance/reflectance measurements are performed for plain alumina membranes in order to determine its n_0 and k_0 values. Nickel volume fraction is determined from the microscopic analysis.

The transmittance after absorption loss for each component of the three layer model shown in Figure 1.9 is given by

$$T_{abs,i} = e^{-4\pi k_i d_i / \lambda} \tag{1.19}$$

where k_i and d_i are the absorption coefficient and optical path length, respectively, for a given layer. The transmittance after reflective losses at each interface in the three-layer model were calculated using

$$T_{R,j} = 1 - \frac{(n_{i+1} - n_i)^2 + (k_{i+1} - k_i)^2}{(n_{i+1} + n_i)^2 + (k_{i+1} + k_i)^2} \; .$$

(1.20)

The total transmittance in the three layer system is given by

$$T_{tot} = \prod_{i=0}^{3} T_{R,i} \prod_{i=1}^{3} T_{abs,i}$$

(1.21)

where i =0 and i =3 pertain to the two interfaces between the host oxide and air.

CHAPTER 2

EXPERIMENTAL SETUP

This chapter explains the structure of the semi-transparent solar selective reflector chosen in this study followed by a brief introduction of the various materials used for the structure. The fabrication process of the coating is discussed, and the characterization techniques used in this study are summarized.

2.1 Semi-transparent Selective Reflector

The structure of the semi-transparent selective reflector fabricated in the study is shown in Figure 2.1. It consists of bare aluminum oxide (commercial alumina membrane) as a host material with nickel nanoparticles deposited inside the pores of the alumina membrane.
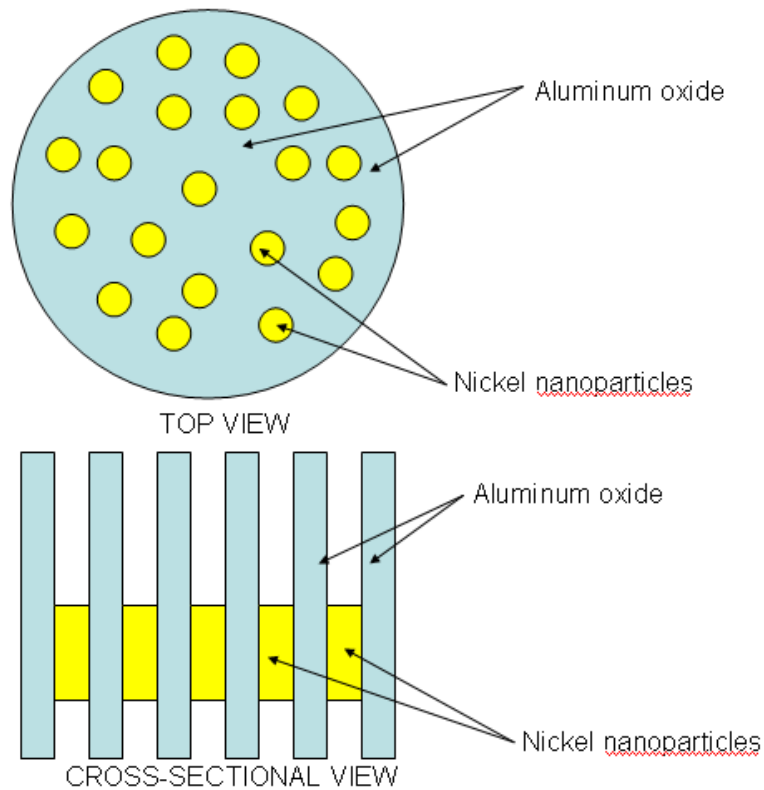
Figure 2.1 Top and cross-sectional views of alumina/nickel selective reflector.

2.2 Aluminum Oxide

Aluminum oxide (Al_2O_3) is an amphoteric oxide of aluminium. It is also referred as alumina. It is optically transparent over a wide range of spectrum (0.3 μm $\leq \lambda \leq$ 6 μm) providing various options for optical applications. Using a porous alumina as a nano-template to fabricate nanometer sized structure has attracted a lot of attention in the field. It has following properties;

(a) It has an ordered array of pores.

(b) Its pore density is in the range of 10^9-10^{12}/cm^2.

(c) The pore diameter ranges from 10 to 400 nm.

(d) The pore length typically varies from 1 to over 100 μm.

(e) It has good thermal and chemical stability.

(f) Low absorption and reflectance in the visible and infrared light range.

The structure of porous alumina is shown in Figure 2.2. For the fabrication of the selective reflector in the study, the commercially available alumina membrane was obtained from Whatman LTD (Figure.2.3). The membrane is normally 60 μm thick and its diameter is about 43 mm. The parallel cylindrical pores in the alumina membrane allow template-synthesized metal nanoparticles homogeneously aligned in one direction. Hence, the collective optical properties of these nanoparticles embedded in the membrane can be systematically studied. The porosity of the membrane is about 50 % and with a burst strength of 65-110 psi. The pore size of the membrane is about 300 nm in diameter.
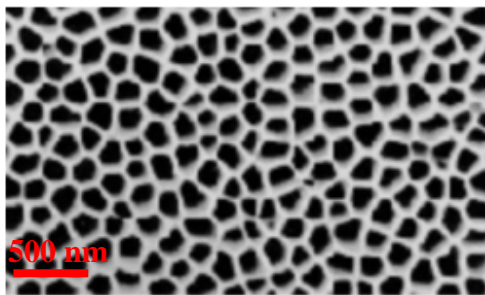
Figure 2.2 SEM top view of commercially available alumina pore structure [26].

Figure 2.3 Top view of commercially available alumina membrane (Whatman Corp, Britain).
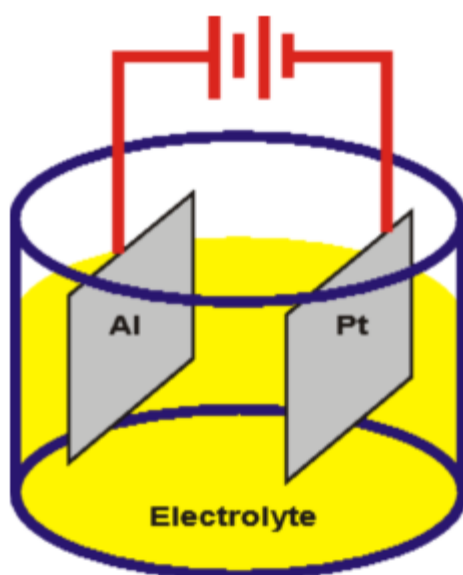
Figure 2.4 Apparatus for anodizing aluminum (13).

Typically the membrane is made by anodizing aluminum in the electrolyte (Figure 2.4). Aluminum oxide growth proceeds via ionic conduction and reaction of aluminum cations and oxygen containing anions under the influence of an applied electrical field (27). The formation

of the pores initiates at random positions through the field-assisted dissolution of the oxide at the oxide/electrolyte interface. There are four steps for the whole anodizing process (Figure 2.5);

(a) Initially, oxide growth on the surface dominates.

(b) Dissolution becomes competitive, barrier layer (the alumina layer between the bottom of pore and aluminum) thins, and pores initiate.

(c) Pores grow and develop.

(d) Approaches steady state where both mechanisms (oxidation and dissolution) occur at roughly the same rate.

Oxide Growth   **Pore Initiation**   **Pore Development**   **Steady State**

I   **II**   **III**   **IV**
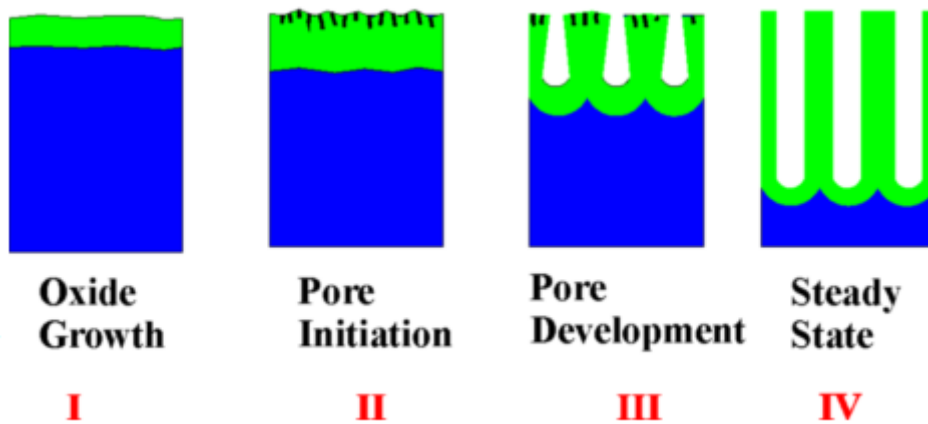
Figure 2.5 Schematic of the anodization process of aluminum (27).

In this thesis we used the commercial alumina membrane which doesn't contain barrier layer and aluminum layer to electrodeposition nickel.

<u>2.3 Nickel</u>

Nickel is a metallic chemical element with the symbol Ni and atomic number 28. It belongs to the transition metals, and it is hard and ductile. In our study, we have selected nickel as our metal component in the selective optical coating due to its high reflectance in the infrared light range (Figure 2.6), the easiness of electrodeposition, relatively high oxidation potential, and

availability of reference data for modeling and calculations. The reflectance curve of nickel in the figure is calculated through the equation (28),

$$R = \frac{(n-1)^2 + \kappa^2}{(n+1)^2 + \kappa^2} \ .$$

(2.1)

The n and κ refer to the refractive index and extinction coefficient respectively and they are from the literature (29).
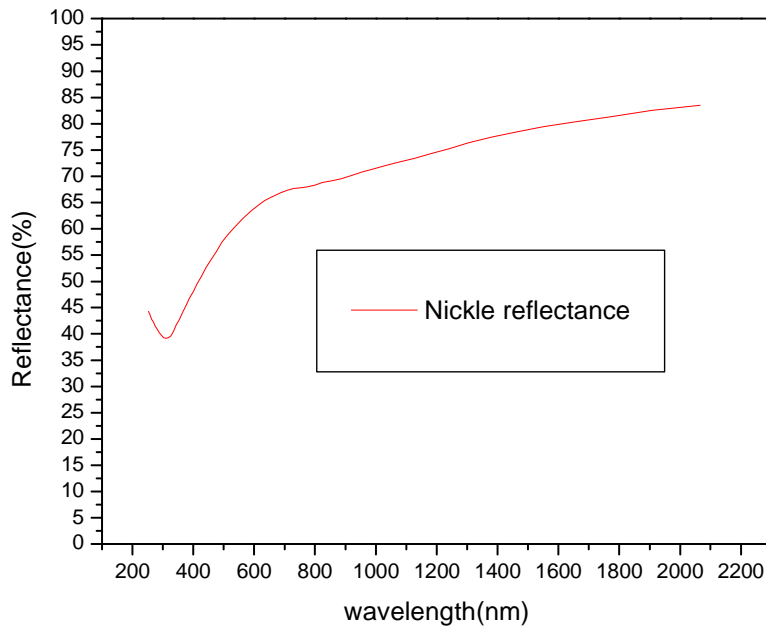
Figure 2.6 The reflectance curve of Ni calculated from reference data (28).

2.4 Fabrication of Alumina/Nickel Selective Optical Coating

Figure 2.7 shows the overall fabrication process of alumina/nickel selective optical coating. First, 1 μm-thick copper layer was deposited on the backside of the membrane using a thermal evaporator to serve as an electrode for the subsequent electrodeposition of nickel. The alumina membrane was used as received and the copper deposition was necessary because alumina membrane is an insulator. After the electrodeposition of nickel, the copper sacrificing

25

layer was dissolved by nickel/copper selective etchant. Each step will be further explained in the following sections.
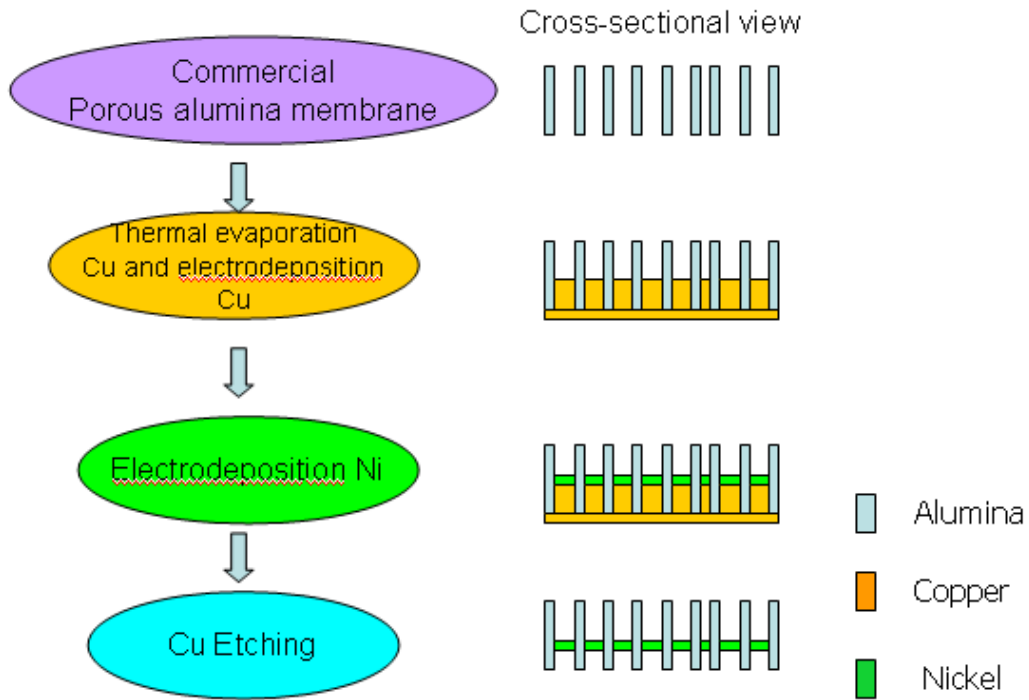
Figure 2.7 Fabrication process of nickel/alumina selective optical coating. In the figure, the light blue block stands for alumina membrane and the orange block is copper and green one is nickel.

2.4.1 Preparing Copper Coated Alumina Membrane for Electrodeposition

Vacuum thermal evaporation of copper pellets (1/8" diameter $\times$ 1/8" length) from Kurt J. Lesker was performed using a home-built thermal evaporator (Figure 2.8) to deposit the copper layer. The base pressure was about 6×10^{-6} torr, and the deposition rate was about 0.4~0.6 nanometer/sec.
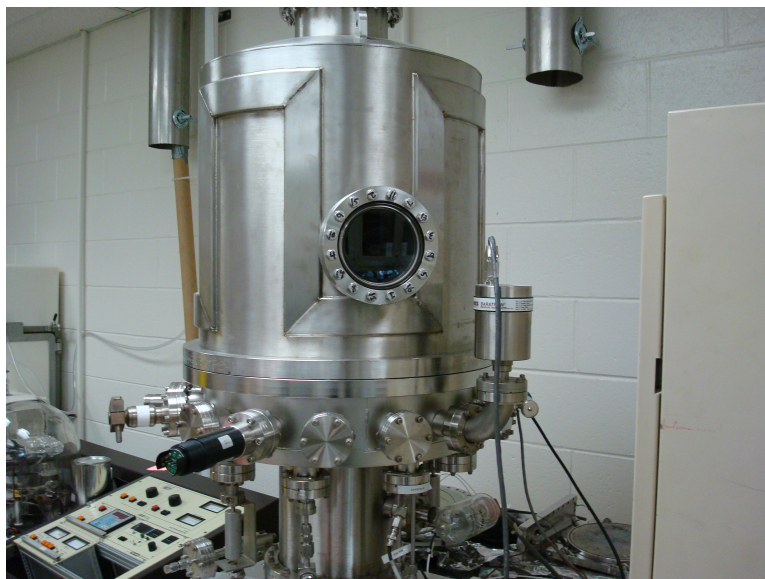
Figure 2.8 Homebuilt thermal evaporator for depositing copper.

2.4.2 Electrodeposition of Nickel

In previously study, people were focused on the optical properties of alumina membrane deposited with thin prolated nickel particle (whose length is larger than the diameter of the particle) deposited in alumina membrane .In this study the alumina membrane deposited with thin oblated nickel particle (whose length is larger than the diameter of the particle) is studied. The four samples with different size of nanoparticles (Table 2.1) were prepared by electrodepositing nickel from baths containing 0.1M $NiSO_4X6H_2O$ and 0.1 M boric acid with pH 3.73 at room temperature. The nanoparticle length was estimated from the nickel deposition rate and deposition time. All solutions in the study were prepared with distilled water. A standard single-compartment, three-electrode cell (Figure 2.9) was used in all the electrochemical experiments, and the electrodeposition experiments were carried out on a 100A Electrochemical Analyzer (Bioanalytical Systems). A Pt coil and a Ag/AgCl saturated KCl probe (Microelectrode Inc.) served as the counter- and reference electrodes respectively, and the process was carried out by potentiostatic deposition at -0.9 V with respect to the Ag/AgCl

27

reference. Before electrodeposition nickel, we first pre-electrodeposition copper for 2minutes to make sure all the holes are covered by the copper.
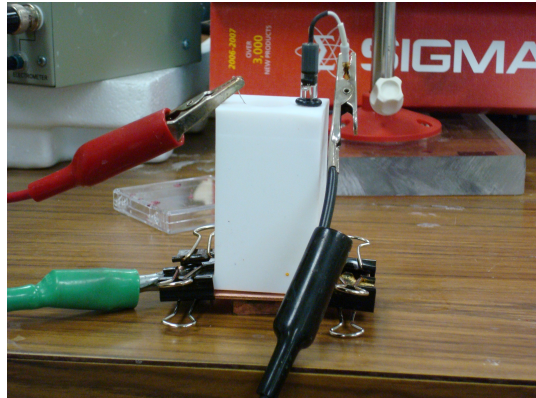
Figure 2.9 Three electrode cell for the electrodeposition of nickel.

Table 2.1 Four selective optical coatings with different nickel particle size.

Sample number	Coulomb (amount of nickel deposition)	Estimated nickel length (nm)
1	0.8	200
2	0.6	150
3	0.4	100
4	0.2	50

2.4.3 Selective Etching of Copper

In order to remove copper layer after the electrodeposition of nickel, the sample was immersed in the copper etchant 49-1 (Transene company INC) for an hour. The sample was rinsed with DI water after etching process and dried by high purity nitrogen gas.

28

<u>2.5 Characterization Techniques</u>

2.5.1 Scanning Electron Microscope (SEM)/Energy Dispersive X-ray Spectroscopic (EDS)

SEM and EDS are crucial to locate the position of the nickel nanoparticles and to measure their size. While the SEM images provide high resolution (16), the EDS provides the elemental analysis. The EDS mapping was performed together with routine elemental analysis in order to investigate the size and the precise location of the nickel particles. The SEM and EDS analysis were performed using a ZEISS Supra 55 VP SEM equipped with a EDS unit from EDAX (Figure 2.10).

Figure 2.10 ZEISS Supra 55 VP scanning electron microscope.

2.5.2 Ultraviolet/Visible/Near IR (UV/VIS/NIR) Spectroscopy

UV/VIS/NIR spectroscopy involves the spectroscopy of photons in the UV/visible/near IR region. In this study, the transmittance and the reflectance of the selective coatings were measured using a Perkin Elmer UV/VIS/NIR spectrometer (Lambda 19) (Figure 2.11).

Figure 2.11 Perkin Elmer UV/VIS/NIR spectrometer (Lambda 19).

2.5.3 Fourier Transform Infrared Spectroscopy (FTIR)

FTIR is a measurement technique which captures the infrared spectra. FTIR is used in this study to measure the transmittance and reflectance of sample in the infrared light range. The spectrometer used in this study (Thermo FTIR Nicolet 6700) is equipped with an IR microscope (Thermo Nic Plan). Transmittance and reflectance were measured by the spectrometer and the microscope respectively (Figure 2.12).
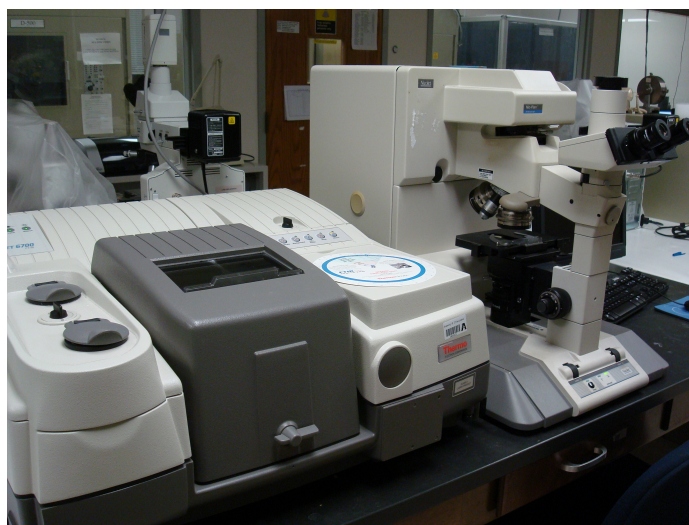
Figure 2.12 FTIR Nicolet 6700 spectrometer and Nic Plan IR microscope for transmittance and reflectance measurement.

CHAPTER 3

RESULTS AND DISCUSSION

In this chapter, the results obtained from various measurements including scanning electron microscopy (SEM), energy-dispersive X-ray spectroscopy (EDS), UV/VIS/NIR spectroscopy and infrared spectroscopy are analyzed and discussed together with simulated results

3.1 Characterization of Ni Particle Size and Location

Figure 3.1 shows the cross-sectional SEM picture of the nickel-deposited alumina template (Sample 1) before dissolving the copper backing-layer. The figure indicates that the copper nanorods were penetrated into the pores of the alumina during copper evaporation process necessary to make the backing layer while some pores were left empty without the presence of the copper nanorod. It is possible that some of the copper nanorods fell off when the sample was sectioned as a part of sample preparation for SEM imaging.
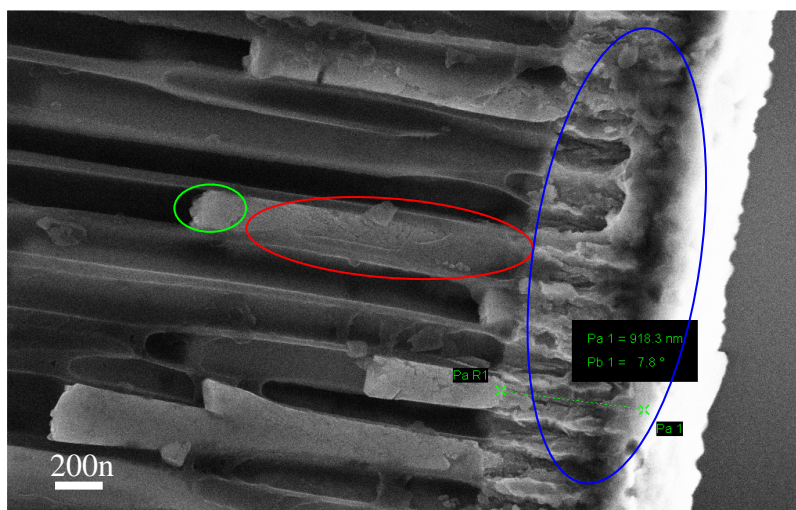
Figure 3.1 Cross–sectional SEM picture of nickel-deposited alumina template with a Cu-backing layer. The green circle indicates the nickel , the red circle shows the copper, and the blue circle shows the alumina template.

The copper backing-layer deposited is on the right side of the picture (blue circle in the figure) and the left part of the figure is alumina template with copper nanorods. The area indicated by a red circle is the copper nanorod which is around 1 to 2 μm and a nickel nanoparticle on top of the copper nanorod is expected to be present and the location is indicated by a green circle. Although the nickel nanoparticles are expected to be found on top of the copper nanorod, it is difficult to probe the existence of the nickel particle directly from the SEM pictures because there was not much contrast difference between Cu and Ni.

In order to analyze the size of the nickel nanoparticles and their location, the mapping function of EDS was used. Figure 3.2 shows the cross-sectional electron images of 4 samples studied and their corresponding EDS images. The set of figures in the left column are electron images and those in the right column are the EDS imaged mapped on the electron images. The black nanorod in the images corresponds to the copper nanorod with the nickel particle on top of it. In the EDS images, the copper nanorod and the nickel nanoparticle are color-coded respectively with yellow and blue. The other area (white part) is made of the alumina template and the size of the pore can be recognized by the contrast difference. The composite images clearly showed the presence of the nickel on top of the copper nanorod providing rough estimate of their size and location. However, EDS imaging did not provide enough spatial resolution to measure the exact size of the particles because the image was not stationary due to the charging effect during the long duration of mapping process – the image of nickel particles from Figures 3.2 (b), (c) and (d) were quite blur while the quality of the image from Figure 3.2 (a) was fairly good because Sample 1 has the largest nickel particles among others.
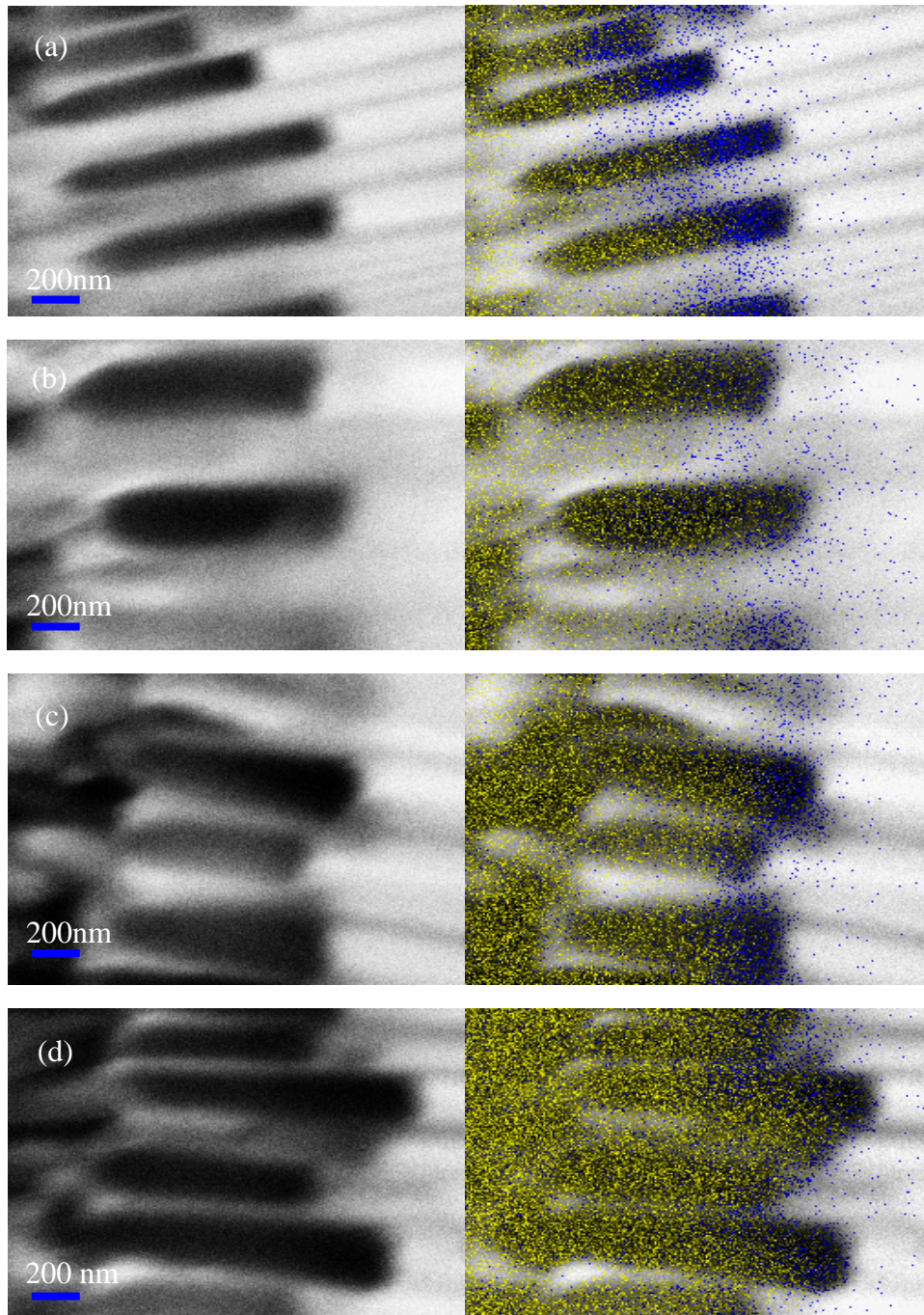
Figure 3.2 Cross-sectional SEM and EDS mapping images of the four samples; (a) Sample 1, (b) Sample 2, (c) Sample 3, and (d) Sample 4. The set of pictures in the left column are electron image and those in the right column are EDS pictures. The copper nanorod and nickel nanoparticle are color-coded respectively with yellow and blue. The white part is alumina.

In order to measure the exact size of the nickel nanoparticles in the alumina membrane, the copper-backing layer was etched away using a copper selective etchant and the samples were studied under a low-vacuum SEM. The signals produced by an SEM include secondary electrons, back scattered electrons and Auger electrons. Most SEM samples are conducting and when the electron beam scanning on it, the specimen will generate secondary electron. For our case, the alumina is dielectric which means when the electron hit the sample, instead of ejection of secondary electron, the electron will be trapped in the specimen which will cause charging. By using the low-vacuum SEM, the secondary image contrast will increase because some electrons will be absorbed by the impurities or water vapor due to low vacuum thus there will be less electron hit on the surface of dielectric and it will decreases the charging in the image though it will lose some resolution. For example, Figure 3.3 shows how nickel particles were identified and measured in Sample 1. Once the nickel particle was found in the cross-sectional SEM image (Figure 3.3(a)), EDS further confirmed the particle's identification by probing the composition of the particle itself and its surrounding. For example, Figure 3.3(b) shows that the EDS spectrum of area B where a particle is discerned showed a nickel peak while it is missing in those of area A and area C. In those EDS spectra, the x axis is energy (eV) and the y axis is an arbitrary intensity.
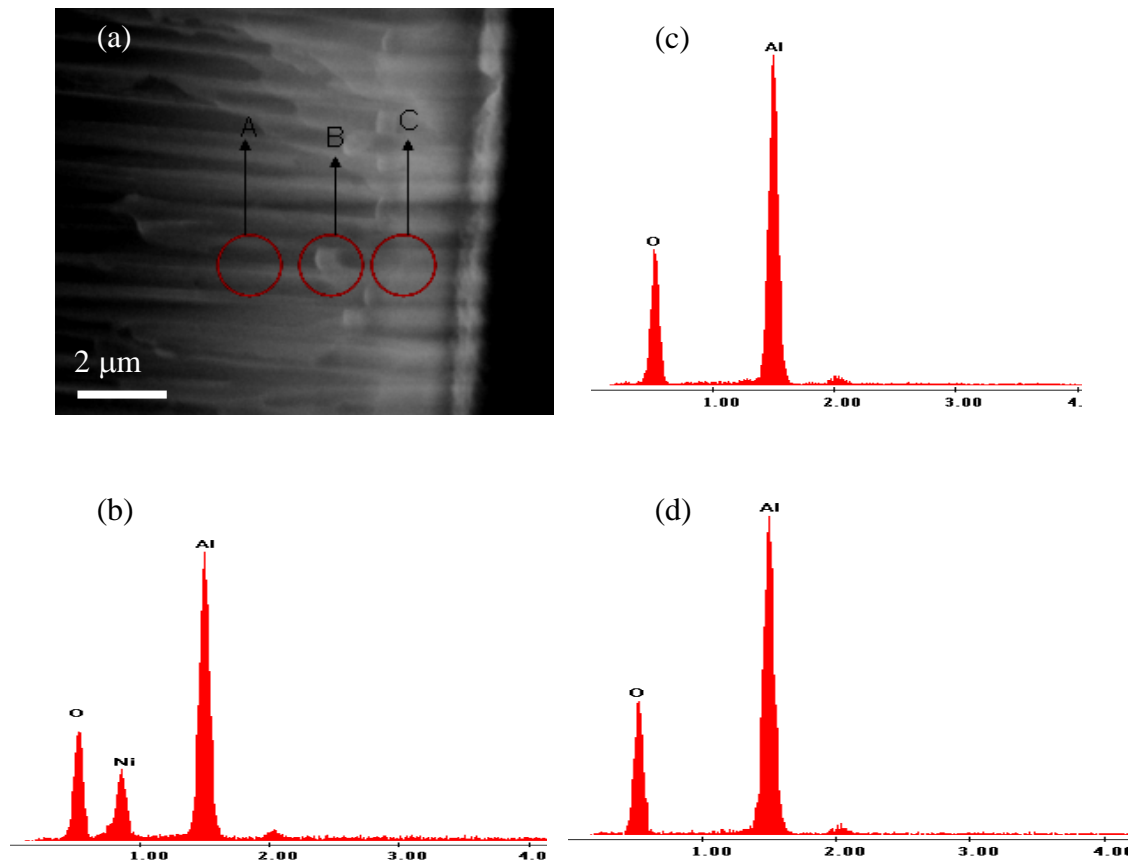
Figure 3.3 A cross-sectional low-vacuum SEM picture (a) and three selective-area ED spectra of Sample 1 (b, c, and d) respectively for three different areas, A, B, and C.

Figure 3.4 shows the cross-sectional low-vacuum SEM pictures of all four samples and the size of nickel particles measured from the micrographs are summarized in Table 3.1. The nickel particle was first positioned using EDS then using the scale to determine the length of the nickel nanoparticle. The nickel particle length summarized in the table 3.1 was the average length of the particle determined from measuring five different particles for each sample. In the figure, the nickel particles were circled (red) and the green arrow shows the length of particle.
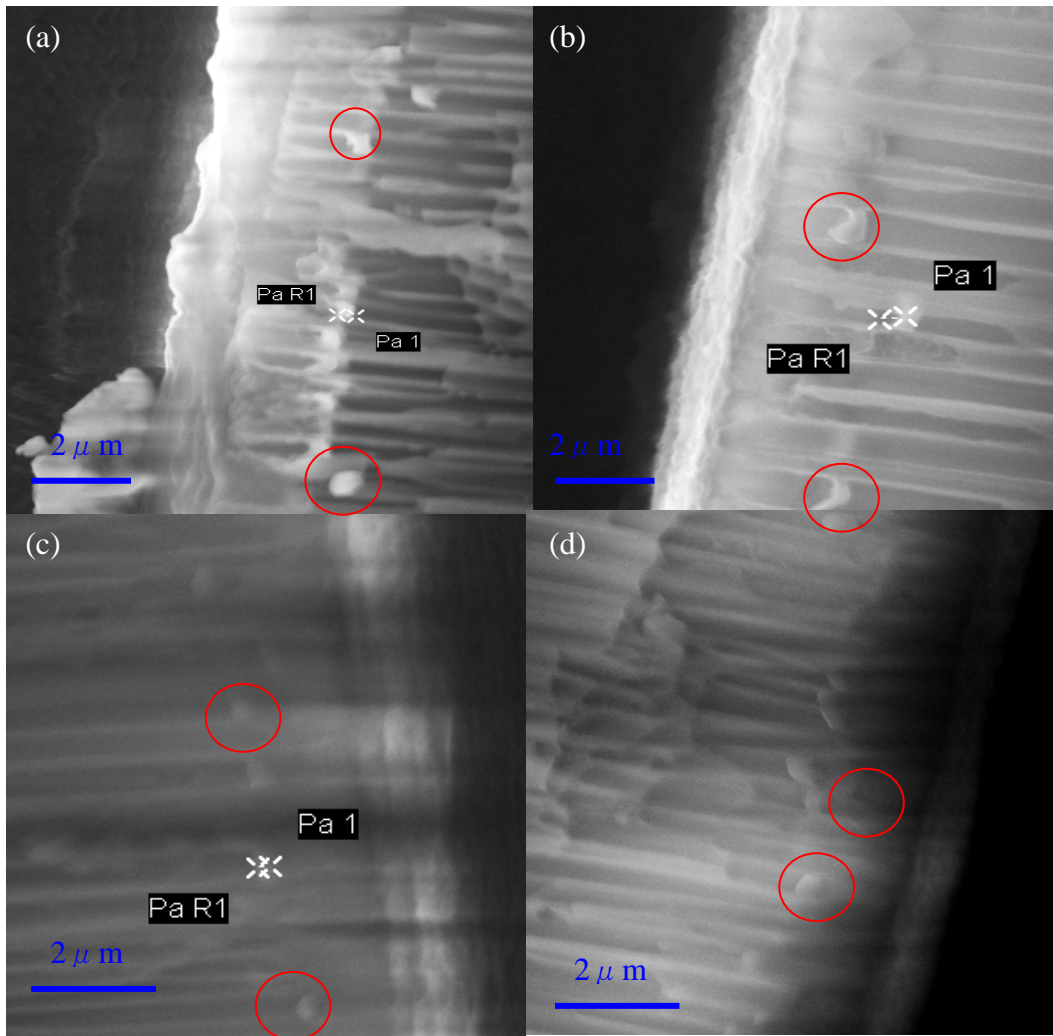
Figure 3.4 A cross-sectional low-vacuum SEM pictures of (a) Sample 1, (b) Sample 2, (c) Sample 3, and (d) Sample 4. The red circle in the picture shows where the nickel nanoparticles located.

The simulation of the optical properties of the nickel/alumina selective optical reflector requires the thickness of nickel-alumina composite layer, D2 described in section 1.5.3. With low -magnification SEM micrographs of the samples prior to the removal of Cu backing layer, D2 was determined by subtracting the length of the shortest copper nanorod (with a nickel

nanoparticle on top) from the length of the longest copper nanorod (also with a nickel nanoparticle on top) in the micrograph taken at a chosen magnification (Figure 3.5). For example, in the figure, the length of the longest copper nanorod is 3.46 μm and the shortest copper nanorod is 2.89 μm. Finally, the D2 is equal to 0.57 μm. The yellow bars in the figure indicate the length of the shortest and the longest copper nanorods. The D2 value is the average of data collected from five different places for each sample. The calculated D2 values for all the samples are summarized in Table 3.1. The expected nickel particle size is calculated from the depositing rate of nickel in the three electrode cell. We first depositing a long nickel nano-rod which is about 2 μ m and we write down the electron amount that used and divided by the time we get a nickel deposion rate. Using this we calculated how much coulomb we need to deposited the desired nickel length. The difference between the expected size of nickel and measured size of nickel can be caused by the nonlinear of the nickel deposition rate. It showed that during the first 0.05 coulomb the the nickel deposition rate keep increasing. And after long time, the nickel deposition rate will go down. The D2 length is decided by the random distribution of copper nanorods. Depending on the position the D2 value will also change but very small.
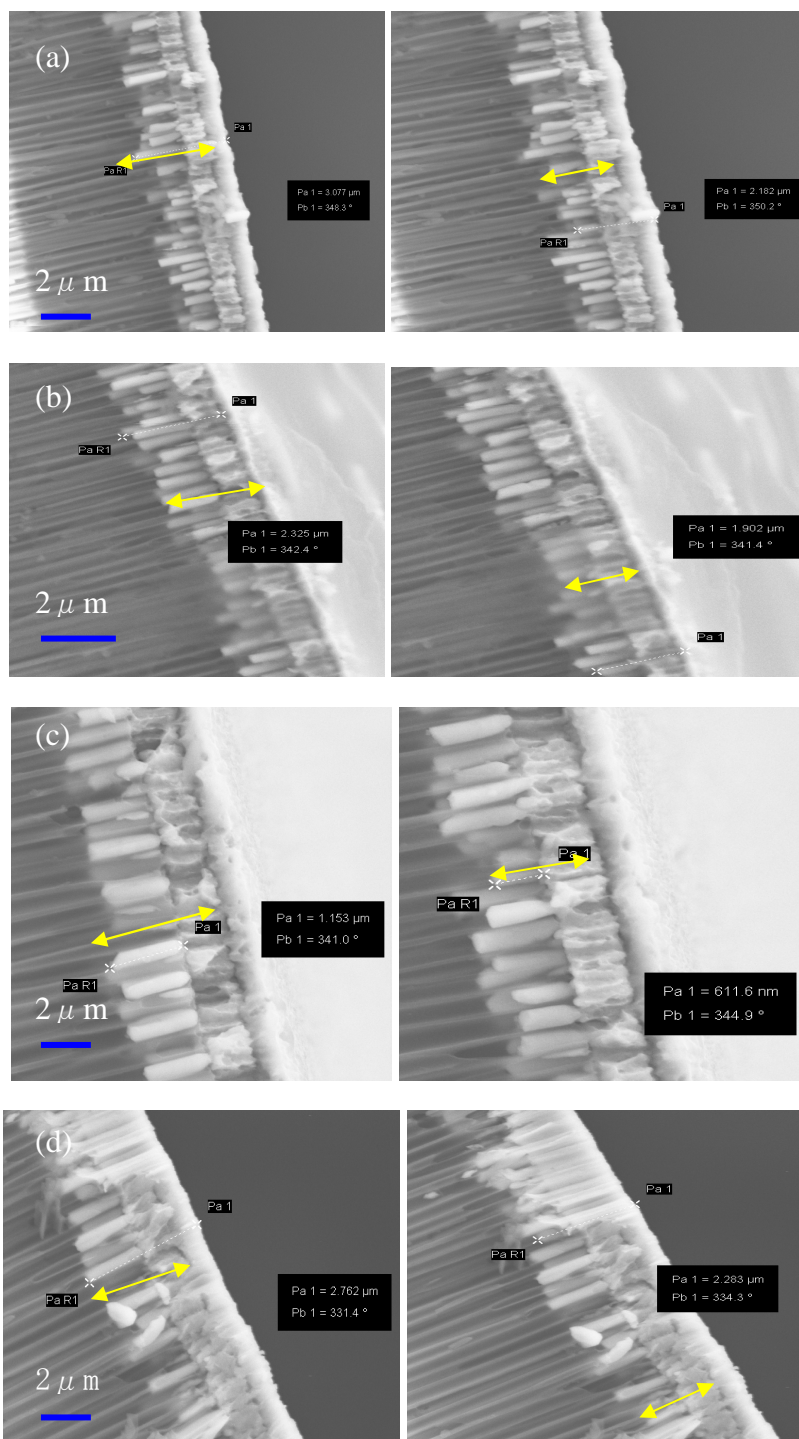
Figure 3.5 Low-magnification, cross-sectional SEM micrographs for the measurement of D2; (a) Sample 1, (b) Sample 2, (c) Sample 3, and (d) Sample 4. The yellow arrow bar shows the longest copper nanorods (left column) and shortest copper nanorods (right column).

Table 3.1 Nickel particle size and optical length of composite layer.

Sample No	Estimated nickel length (nm)	Measured nickel length (nm)	D2(μm)
1	250	245	0.667
2	187	150	0.97
3	125	130	0.675
4	63	109	0.804

Figure 3.6 shows the top-view SEM micrographs of the four samples after etching away the Cu backing layer. Here we want to make sure whether all the holes are deposited by the nickel nanoparticles because later in the simulation part, we suppose that all the holes are blocked by nickel nanoparticles. The figure shows that there are both black holes and light white holes in the figure. By using the EDS analysis on the black hole and light white hole, we found that not all the alumina holes are filled with the nickel particles. The black hole in the figure indicates there is no nickel in the hole and the light white hole indicates the presence of the nickel particle. As we can see from the figure that hole concentration goes up from sample 1 to sample 4. This is because the amount of the nickel deposition is decreased from sample 1 to sample 4 and as the nickel deposition amount decrease there will be more chance that the alumina pores are not covered by the nickel. The implication of the empty holes will be further discussed in the following sections. The concentration of the hole is measured by the total area of empty holes in the figure divided by the total area of the alumina template. The calculated vacancy concentration is summarized in Table 3.2, which will be further discussed together with optical analysis in the next section.
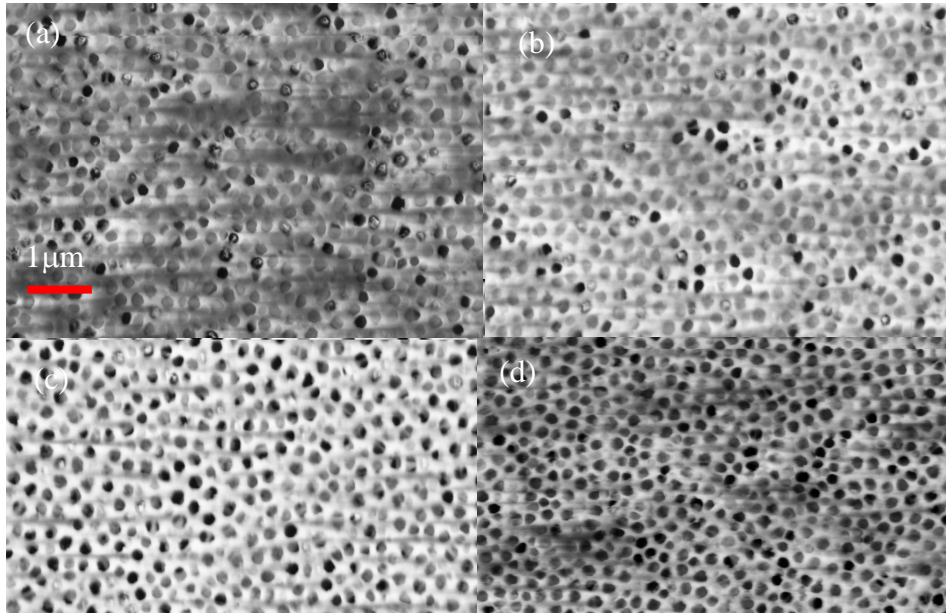
Figure 3.6 Top-view SEM microscopes of the four samples (a) sample 1 (b) sample 2 (c) sample 3, and (d) sample 4 after Cu etching.

<u>3.2 Optical Analysis of Alumina/Nickel Selective Reflector</u>

Both UV/VIS/NIR and FTIR spectroscopies were used to measure the transmittance and reflectance of the alumina/nickel selective reflector samples in the spectral range from 200 nm to 5000 nm. Figure 3.7 shows the transmittance/reflectance curves of the four different samples together with bare alumina template. While the bare alumina template shows very high (70 – 90 %) transmittance in the entire spectral range, the transmittance of the sample with the biggest (245 nm) Ni particles (sample 1) shows the lowest level of transmittance. Overall, as the amount nickel deposition increased, the transmittance has decreased.

The transmittance and reflectance curves in the IR range show some continuous wave crest and trough. This is caused by IR light interference. The intensity of the interference in the transmittance spectrum and reflectance spectrum is different. Because the interference of light rays observed from reflections off a film are different than the interference from transmitted light (figure 3.8). The two reflected rays (I_1^r , I_2^r) are almost the same intensity, while the two transmitted light are of much different intensities (30). Constructive interference between two rays of the same wavelength occurs when the light traveled an integral multiple of the wavelength with respect to the other ray and destructive interference occurs when the path difference is a half integral multiple of the wavelength. In the transmittance curve, curve goes down as nickel size gets bigger because of the increased light absorption/reflection by the nickel particle. It also clearly shows that as the nickel deposition amount increases the reflectance of the composite increases. This is reasonable according to the effective medium theory, once we increase the nickel size and its volume fraction, the final refractive index of the composite will increase. But simply increase the nickel amount will decrease the transmittance of the reflector. That is not what we want and future work will focus on trying transparent conducting oxide to make the reflector.
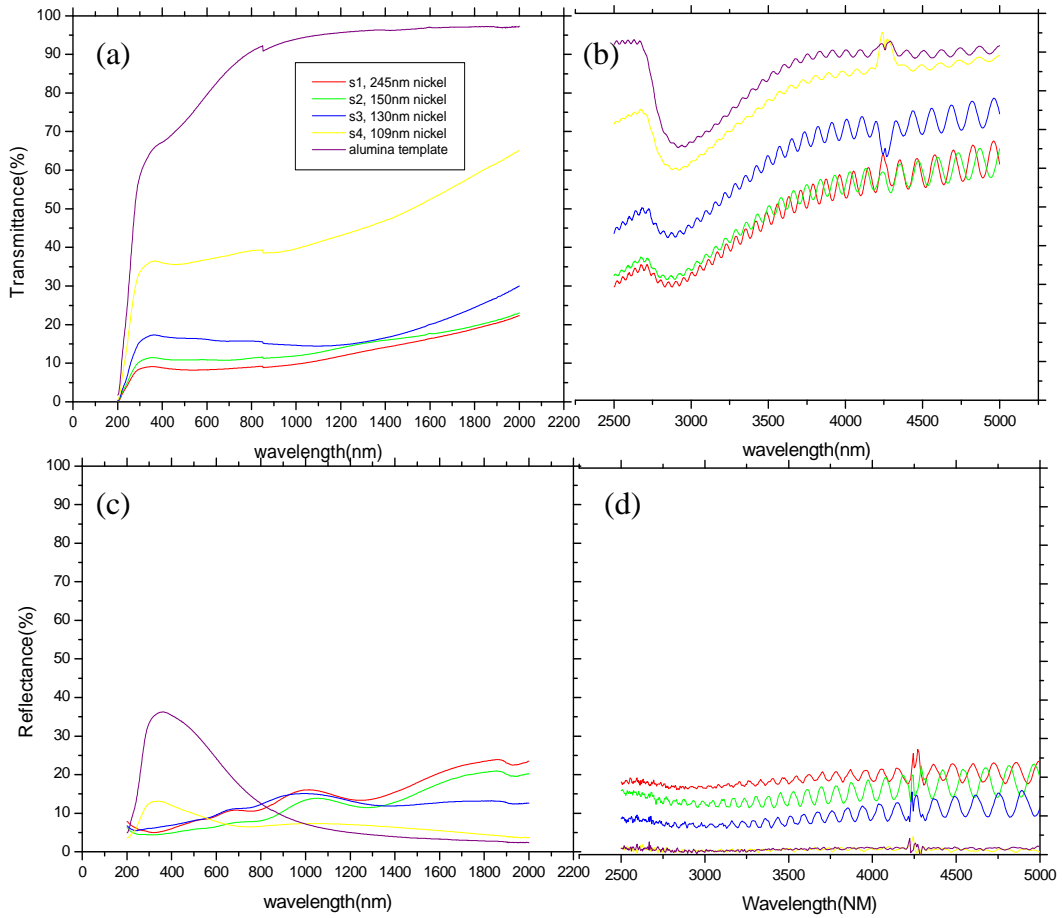
Figure 3.7 Optical measurements of alumina/nickel selective reflectors; (a) the transmittance curve of four different samples together with a bare alumina template in the UV/VIS/NIR spectrum (b) transmittance curve of four samples and bare alumina template in the IR spectrum (c) reflectance curve of four samples and bare alumina template in the UV/VIS/NIR spectrum and (d) reflectance curve of four samples and bare alumina in the IR spectrum.
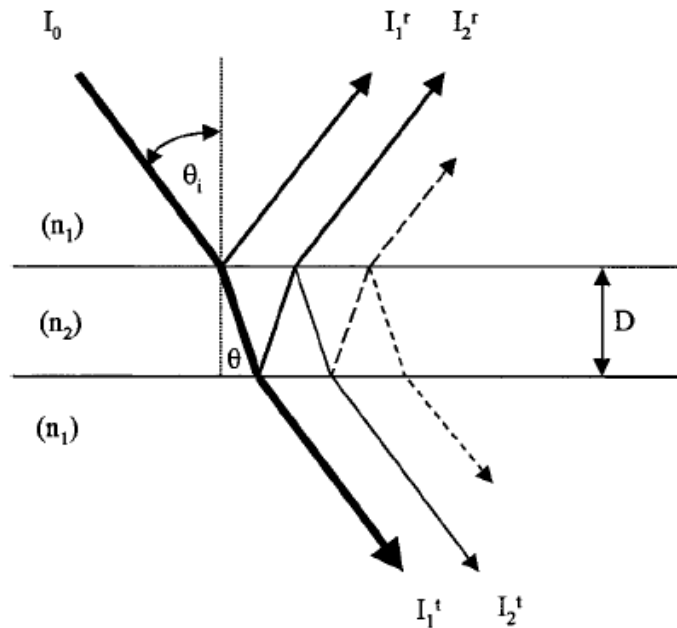
Figure 3.8 Interference caused by light traveling different paths through a film.

3.3 Optical Simulation

In this section, MG theory was applied to calculate the optical constant of the nickel/alumina composite layer in order to simulate the optical spectra of the four samples and compare with the measurements.

Through SEM pictures, the deposited nickel nanoparticle length and D2 were characterized and summarized in table 3.1. By applying the effective medium theory and the equations 1.14, 1.15, 1.16, 1.17 and 1.21, the transmittance curves of the four samples were simulated (figure 3.9). In Figure 3.10, the total transmittance of Sample 1 was deconvoluted into the transmittance after absorption loss and the transmittance after reflectance loss. The figure shows that the absorption loss plays a dominant role in the total transmittance. However, comparing the experiment data in the figure 3.7a with the simulated data in the figure 3.9 indicated that the simulated plots do not show any agreement with the experiment data. In the near IR spectral range, the simulated curve was quite higher than the measured data and in the

43

visible spectral range the simulated data do not show any transmittance at all. In the near IR range, the simulation underestimated absorption caused by nickel nanoparticles and in the UV and visible light range the nickel absorption effect is overestimated. In addition, the SEM picture (figure 3.6) showed that the not all the alumina pores were filled by the nickel nanoparticles and the MG theory needs some modification. Because the light can almost completely pass through the holes without nickel particle, we assume that the light pass through the empty holes without any loss and the transmittance of the left part of the membrane will be explained by using MG theory to calculate.   Another point we need to consider is that when the light passes through the pores of the membrane, it is possible to have multi reflection and absorption. While the real volume fraction of the nickel can be calculated from their size, the effective volume fraction of nickel can be defined to explain the low transmittance due to multi absorption and this effective volume fraction should be bigger than the calculated volume fraction. Based on the discussions above, the following modifications were made in the simulated transmittance curves.
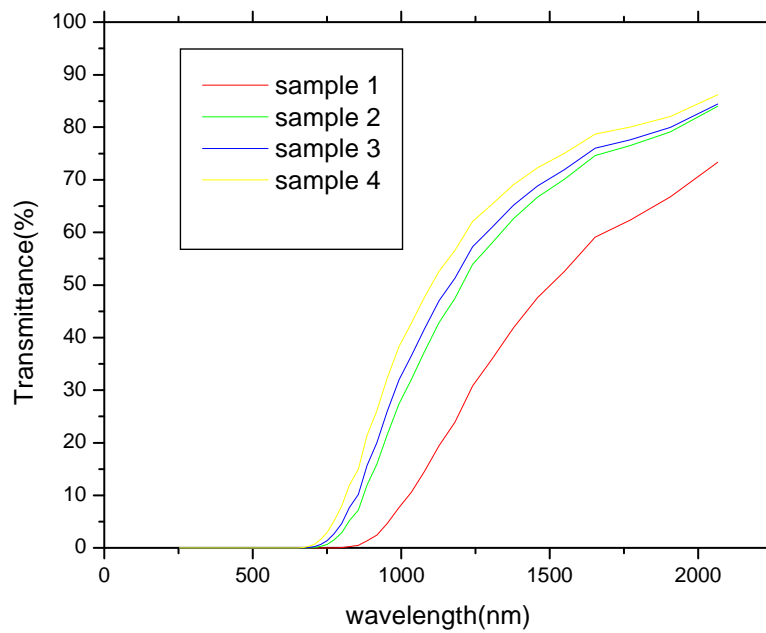
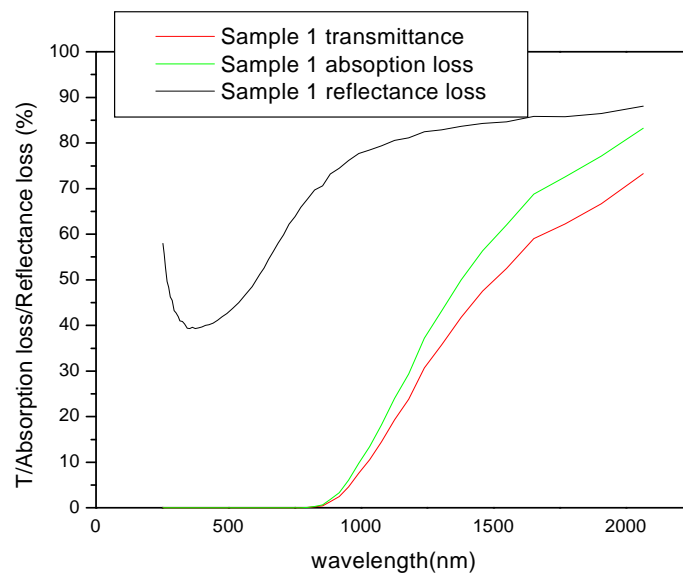Figure 3.9 Transmittance curve of four samples using MG theory.

Figure 3.10 Simulated transmittance curve of sample 1 (red line) and its corresponding absorption loss (green line) and reflectance loss (black line).
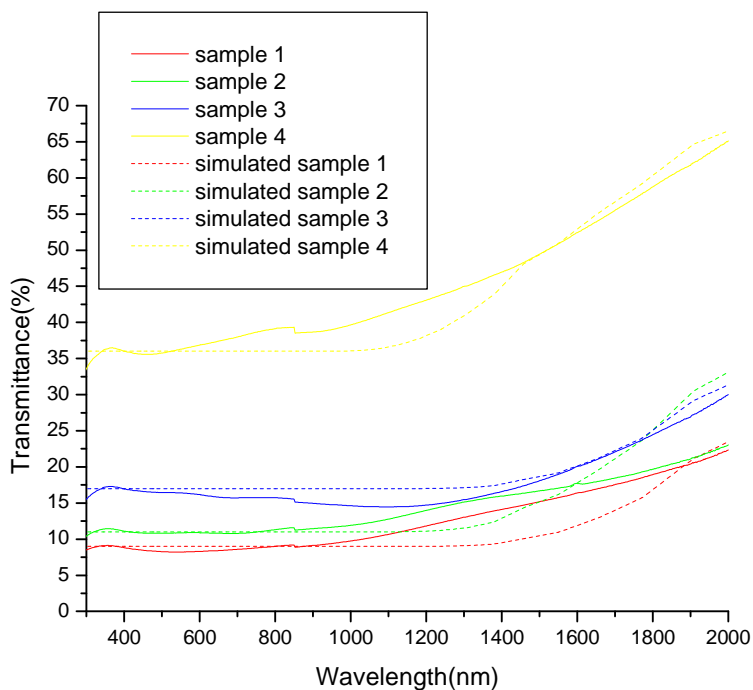
Figure 3.11 Comparison between the experimental (solid) and caculated (dashed) UV/VIS/NIR spectra.

First we calculate the concentration of the holes without nickel particles and assume the light will pass through the empty holes without any loss. The first column of the table 3.2 shows the concentration of empty holes determined from SEM picture. This is done by calculating the total area of empty holes in the figure divided by the total area of the alumina template The second column of the table 3.2 shows the hole concentration extracted from experiment result. The calculated result and extracted result are different because the calculated hole concentration is just a part of the membrane. Thus there will be some deviation.

Secondly, according to the multiple light absorption and multiple light reflection, we reextracted the effective f_m value (volume fraction of nickel) from the experiment data in order to simulate a transmittance curve in the overall spectrum range. The third column of the table 3.2 shows the nickel volume fraction calculated from experiment. The numbers in column three does not increase in one direction. This is because the volume fraction depends on both nickel

46

nanoparticle size and optical length of the composite layer. Although the nickel particle size increases as we increase the deposition time the optical length of the composite (D2) is uncontrollable. D2 is a random distribution of copper nanorods. The fourth column shows the effective nickel volume fraction which is extracted from fitting experiment data. By comparison between the third column and fourth column, it obvious that the effective f_m are much larger than the calculated nickel volume fraction. This can be explained by the multiple light absorption and multiple light reflection.

Figure 3.11 shows the comparison between the experimental transmittance curve from UV/VIS/NIR and the calculation based on the MG theory with the modifications we made. As we can see from the figure, the simulated data shows very good agreement with the experiment data. In some visible light range, there is still some deviation compared to the experiment data. We think this is because the refractive index and absorption coefficient of nano-scale nickel are different from the literature values that are from the bulk nickel. As the nickel size becomes smaller and smaller, the absorption peak of the nickel will blue shift due to quantum size effect. As the absorption peak shifts, it means the refractive index and extinction coefficient of nickel changes.

Table 3.2 Concentration of empty holes and the volume fraction of metal nanoparticle.

Sample No	Concentration of empty holes determined from SEM	Concentration of empty holes determined by fitting	f_m from the size of particles	Effective f_m extracted from fitting experimental data
1	11%	9%	0.268	0.64
2	9%	12%	0.236	0.6
3	26%	18%	0.278	0.66
4	54%	38%	0.213	0.5

3.4 Conclusion

A novel way of fabricating spectrally selective solar reflector was investigated and developed. The reflector is a part of photovoltaic thermal window application and it need to transmit visible light while reflecting mid/far infrared light back into the window in order to minimize infrared radiative loss. The solar selective reflector studied consists of oblated nickel nanoparticles in alumina matrix – the particles have a disk shape with a diameter of 300 nm and it length varies from about 100 nm to 200 nm. The oblated particles are expected to provide high transmission in visible spectrum because when the light hit the surface of the nanoparticle the prolated nanoparticle will generate more depolarization field compared to the oblated nanoparticle. Thus the oblated structure will be better for light transmission.

Electrodeposition method is used to deposited nickel nanoparticles due to its simplicity and their size was controlled by the deposition time. The surface and cross sectional morphology were characterized by a series of SEM and EDS measurments and the optical properties are analyzed by UV/VIS/NIR and FTIR spectroscopies.

Measured optical data was fitted by employing Maxwell-Garnett effective medium theory which allows calculating the optical constants of the composite. Simply apply the Maxwell-Garnett theory doesn't explain well for the experiment data. In the near IR spectral range, the simulated curve was quite higher than the measured data and in the visible spectral range the simulated data do not show any transmittance at all. Fairly good agreement between measured transmittance and simulated data was made by considering the number of pores without Ni nanoparticles, multiple light absorption, and multiple light reflection. The effective volume fraction was extracted during the fitting process,

The future study includes generating a universal equation that accounts for the multiple absorption/reflection of the effective medium. The results from this study indicate transparent conducting oxide could be a good candidate for the solar selective reflector coating because the transparent conducting oxide is transparent to the visible light and the plasmon absorption peak

is around 2000nm which means it has very good selective reflectivity for Photovoltaic thermal application because the light with wavelength larger than 2000nm will be reflected.

REFERENCES

[1] Kreider and Kreith, Solar heating and cooling: engineering, practical design (1975).

[2] A.Contreras, , J. Carpio, M. Molero, and T.N. Veziroglu "Solar-hydrogen: an energy system for sustainable development in Spain." International Journal of Hydrogen Energy 24, no. 11 1041-1052, (1999).

[3] M.Bakker, W. V.Helden, H.Zondag Energy Research Center of the Netherlands ECN, "PVT RESEARCH AT ECN",Paper presented at European conference and cooperation exchange on sustainable energy systems for buildings and regions, (2005)

[4] J,Jie, C.Tin-Tai, H. Wei. Dynamic performance of hybrid photovoltaic/thermal collector wall in Hong Kong. Building and Environment, Vol. 38(11), 1327-1334, (2003),

[5] H.A. Zondag, W.G.J. van Helden, M.Bakker, " D 3-5: PV-Thermal systems marketing and R&D roadmap"., Derliverable of the EU Project PV Catapult 502775 Energy Research Center of the Netherlands ECN ,(2006)

[6] C.G Granqvist, Spectrally Selective Surfaces for Heating and Cooling Applications. The International Society for Optical Engineering, Washington, (1989).

[7] O.P. Agnihotri and B.K. Gupta, Solar Selective Surfaces. John Wiley & Sons, New York,89, (1981).

[8] J.Gordon, ,ed. 2001. Solar Energy, The State of the Art. James & James Ltd: London.

[9] T. Boström, Design of a solar thermal system with high solar fraction in an extremely well insulated house. In Proceedings of ISES. (2003)

[10] G. A. Niklasson, C. G. Granqvist, and O. Hunderi, Effective Medium Models for the Optical Properties of Inhomogeneous Materials, Appl. Opt. 20, 26-30 (1981).

[11] Atkins, P.W.Physical Chemistry, 2nd ed.; W.H. Freeman; Sanfrancisco, 772-773, (1982)

[12] M.R Nejati, V.Fathollahi Solar collector materials, state of art and further development

[13] Mar, H.Y.B. and J.H., Liu, Optical Coatings for Flat Plate Solar collectors, (1975)

[14] F.Granich and E. Sailer , Sol Energy Mater, 20, ,81, (1990)

[15] Q.C.Zhang and D.R. Mills ,J Appl.Phys.,72, ,3013-3021, (1992)

[16] A. Foss Colby Jr, J. Tierney Michael, R. Martin Charles, J. Phys. Chem. 96, 9001 (1992);

[17] W.G.Driscoll, and W. Vaughan, Handbook of optics. (1978).

[18] D.R. Lide, CRC handbook of chemistry and physics (77th edn), (1996).

[19] Buckley, A.R.,Rahn, M.D.,Hill, J., Cabanillas-Gonzales, J., Fox, A.M.and Bradley, D.D.C. Chem. Phys.Lett.,339-331 (2001).

[20] D.E. McCarthy, Applied Optics, 6. 1986.

[21] D.E. Aspnes,Thin Solid films,89,249, (1982)

[22] J.C.M.Garnett,Philos.Trans.R.Soc.(london)203,385(1904),205,237(1906).

[23] D.A.G.Bruggeman, Ann.Phys.(Leipzig) 24 ,636 (1935)

[24] G. L.Hornyak, J. D, Hrry and F.Tibbals , Introduction to Nanoscience 278-279,(2005)

[25] D. W. Lynch and W.R. Hunter, in Handbook of Optical Constants of Solids, (1975)

[26] http://www.whatman.com/PRODAnoporeInorganicMembranes.aspx

[27] V.P. Parkhutik, and V.I. Shershulsky, J. Phys. D:Appl. Phys. 25, 1258 (1992).

[28] M.Fox, Optical properties of solids , 7-8

[29] D. W. Lynch and W.R. Hunter, in Handbook of Optical Constants of Solids, (1975)

[30] P. D.T.Huibers and D. O. Shah, Languir, 13, 5995-5998, (1997)

BIOGRAPHICAL INFORMATION

Xin Wang was born in Shanghai, China. He completed his Bachelor of Science in Electronic Science and Technology from Fudan University, Shanghai, China.

In fall 2005, he joined Materials Science and Engineering as a graduate student to obtain Master's Degree. He worked as a graduate research assistant in the Photovoltaics Materials Laboratory for three years. After completion of Master's degree, he will look for an engineering position in a semiconductor company.